

This item is the archived peer-reviewed author-version of:

Biomimetic sonar : binaural 3D localization using artificial bat pinnae

Reference:

Schillebeeckx Filips, de Mey Fons, Vanderelst Dieter, Peremans Herbert.- Biomimetic sonar : binaural 3D localization using artificial bat pinnae
The international journal of robotics research / Massachusetts Institute of Technology - ISSN 0278-3649 - 30:8(2011), p. 975-987
Full text (Publisher's DOI): <https://doi.org/10.1177/0278364910380474>
To cite this reference: <https://hdl.handle.net/10067/861330151162165141>

Biomimetic Sonar: Binaural 3D-Localization using Artificial Bat Pinnae

Filips Schillebeeckx
Dep. of Math. and Comp. Science
Univ. of Antwerp, Belgium
Filips.Schillebeeckx@ua.ac.be

Dieter Vanderelst
Dept. of Biology
Univ. of Antwerp, Belgium
Dieter.Vanderelst@ua.ac.be

Fons De Mey
Dep. of Math. and Comp. Science
Univ. of Antwerp, Belgium
Fons.Demey@ua.ac.be

Herbert Peremans
Dept. MTT, Fac. of TEW
Univ. of Antwerp, Belgium
Herbert.Peremans@ua.ac.be

May 7, 2010

Abstract

This paper presents an advanced bio-inspired binaural sonar sensor capable of localizing reflectors in 3D-space with a single reading. The technique makes use of broadband spectral cues in the received echoes only. Two artificial pinnae act as complex direction-dependent spectral filters on the echoes returning from the insonified reflector, thereby adding a spatial signature to the echo spectrum. The 'active head-related transfer function' (AHRTF) is introduced to describe this spectral filtering as a function of the reflector angle, taking into account the transmitter radiation pattern, both pinnae and the particular sonar head geometry. 3D-localization is performed by selecting the azimuth-elevation pair with the highest a posteriori probability, given the binaural target echo spectrum. Experimental 3D-localization results of a ball reflector show that the AHRTF carries sufficient information to discriminate between different reflector locations in significant noise conditions. Experiments with two more complex reflectors illustrate that the spatial signature dominates the resulting echo spectrum, allowing 3D-localization in the presence of spectrum distortions caused by reflector filtering. This sonar device with artificial pinnae provides a large information rate compared to conventional sonar systems.

1 Introduction

In robot applications, sonar sensing is rarely used beyond simple tasks such as obstacle avoidance. This study intends to show that advanced sonar can provide a robot with useful scene information. In the past, doubts have been rightfully expressed on the performance level of non-advanced sonar sensors (Thrun 2001). The same study however points out that "having access to 3D-information should facilitate a range of hard estimation problems, such as the data association problem in mapping".

Advanced 2D-sonar sensors have been developed that surpass the limitations of the widely-used Polaroid Ranging Module (Biber, Ellin, Shenk & Stempeck 1980). Sonar data has been used for robust mapping and indoor localization in indoor environments (Tardos, Neira, Newman & Leonard 2002), and this study notes "one avenue for research to overcome difficulties with sonar data is to develop advanced sensor arrays that allow feature discrimination and precise localization from a single vehicle location". Advanced 2D-sonar systems based on time-of-flight measurements capable of single cycle classification of planes, corners and edges have been reported (Kleeman 2004), (Chong & Kleeman 1999a), (Chong & Kleeman 1999b). By sweeping a narrow-beam sonar sensor over extended objects, walls, fences and hedges can be distinguished (Gao & Hinders 2006). Intelligent processing enables map

building of indoor environments from such ultrasonic arc maps (Barshan 2007), (Ayrulu & Barshan 1998), although this approach requires a lot of measurements. The complementary approach presented here extracts scene information from a single wide-beam broadband measurement. This study shows that it is possible to localize realistic objects in 3D-space with a binaural bio-inspired sonar head, using fairly simple technology and a straightforward probabilistic method.

Because of the stark contrast with the limited capabilities of current robotic sonar systems, the ability of echolocating bats to navigate and hunt in complete darkness has intrigued sonar system developers for a long time, and continues to do so (Müller & Kuc 2007). Performing these navigation tasks skillfully requires successful target localization in 3D-space. While distance to a target is readily calculated from travel time and speed of sound, estimating a target angle (azimuth θ and elevation ϕ) is a much harder task.

The majority of technical systems that have tried to solve this localization subtask use triangulation methods based on ITD-cues i.e., interaural time difference (Barshan & Kuc 1992), (Peremans, Audenaert & Van Campenhout 1993), (Kuc 1993), (Kleeman & Kuc 1995), (Barshan & Sekmen 1999). **The localization performance of such systems improves with increasing interaural time differences, often realized by increasing the interaural distance. However, trading intensity for time, the introduction of a non-zero vergence angle between receivers (Kuc 2002) might alleviate this problem. More importantly however, ITD-cues available to a binaural system only allow angle estimation in the microphone plane (Shinn-Cunningham, Santarelli & Kopco 2000). Indeed, unambiguous angle estimation in the perpendicular plane would require a third receiver (Akbarally & Kleeman 1995). A binaural system requires cues other than ITD to localize reflectors in 3D-space.**

Experiments have shown that echolocating bats use information extracted from the systematic variations in the spectrum of the received echo, depending on the reflecting target location, as localization cues (Wotton & Simmons 2000). Some recent studies have proposed ways of using these spectral cues for target localization. In (Keyrouz, Diepold & Keyrouz 2007) and (Rodemann, Ince, Joublin & Goerick 2008) passive hearing is used to determine the angular position of an unknown sound source. Active sonar systems, for which the spectral content of the emitted call is known, have been studied (Altes 1978), but these studies have

been limited to simulation and theoretical results. In (Abdalla & Horiuchi 2008) spectral cues are used to localize a known emitted call, directly aimed at the receiving binaural head. None of these systems have shown 3D-localization of real reflectors with a single, binaural, active sonar measurement in realistic noise conditions.

The basic idea of spectral influence of beam patterns was reported in (Kuc 1994). Previous work has described how a binaural system based on Polaroid transducers can extract a target range and azimuth i.e., 2D-position, from spectral information only (Reijniers & Peremans 2007). Taking inspiration from biosonar, two strategies to extend this approach to full 3D-localization become apparent. Experimental data shows that real bat sonar systems have both a considerably more complex directivity (De Mey, Reijniers, Peremans, Otani & Firzlauff 2008) as well as, depending on the species, the capability to move their outer ears during measurements (Pye, Flinn & Pye 1962). While a technique using the latter approach has already been demonstrated (Peremans, Walker & Hallam 1998), it requires multiple measurements. This paper adopts the first strategy i.e., build a sensor system with a more complex directivity to improve the system's ability to localize a reflector.

Building a small sonar device requires transducers that are much smaller than the widely-used Polaroid transducers, but such transducers (e.g. the Knowles FG-23329 used in this research) are virtually omnidirectional (Kinsler, Frey, Coppens & Sanders 2000) and therefore lack the required spatial directivity characteristics. In order to enhance their fitness for localization tasks, it is necessary to artificially improve the spatial directivity characteristics of the receivers. Interestingly, the complex spatial filtering of various bat pinnae has been extensively described to do just that (Obrist, Fenton, Eger & Schlegel 1993). Inspired by its biological counterpart, we have mimicked this approach in the sonar device presented here.

In section II, we shortly describe the biomimetic sonar system and the spectral code extraction method. Next, we analyze the directivity pattern of a single artificial pinna. In section IV, we introduce the concept of the active head related transfer function (AHRTF) and investigate its direction-dependent spectral effects on reflector echoes. Section V describes the probabilistic 3D-localization method. Section VI presents experimental results of this 3D-localization method on different reflectors. Lastly, we discuss the results and draw conclusions.

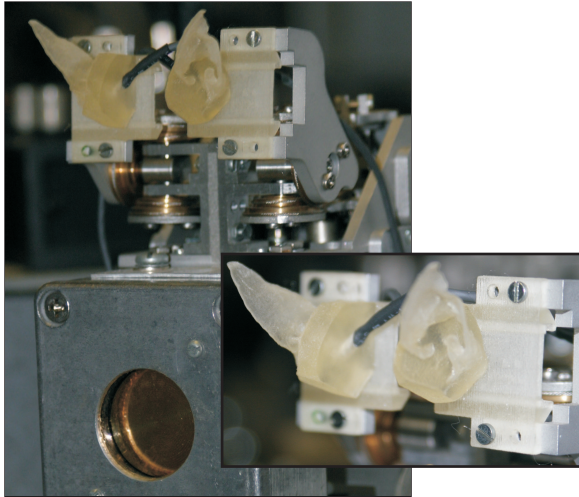


Figure 1: Circe sonar head with two artificial *Phyllostomus discolor* pinnae and Polaroid emitter. Right: close-up of the 3D-printed *Phyllostomus discolor* pinnae

2 Biomimetic Sonar System

2.1 The Robotic Bat Head

The Circe head (fig. 1) was developed to reproduce, at a functional level, the echolocation system of bats (Peremans & Reijniers 2005). Two receiver-assemblies can be mounted onto a small cable mechanism that allows accurate independent control of both receiver orientations. However, in the experiments described below, the two receiver assemblies remained in a fixed position with respect to the transmitter. The distance between the receiver centers in this configuration was 25 mm. The sonar head is mounted on a 'neck' platform which can be panned between -45° and $+45^\circ$ and tilted between -36° and $+36^\circ$ (full range). By fixing a reflector in front of the head, its angle (azimuth, elevation) with respect to the sonar head can be accurately controlled. The transmitter (**Polaroid Series 7000 electrostatic transducer - diameter $d=2,5\text{cm}$**) is part of the sonar head i.e., for each head orientation the sound energy is primarily directed in the corresponding direction. Fig. 2 shows a schematic of the measurement setup and the angle conventions used throughout the paper.

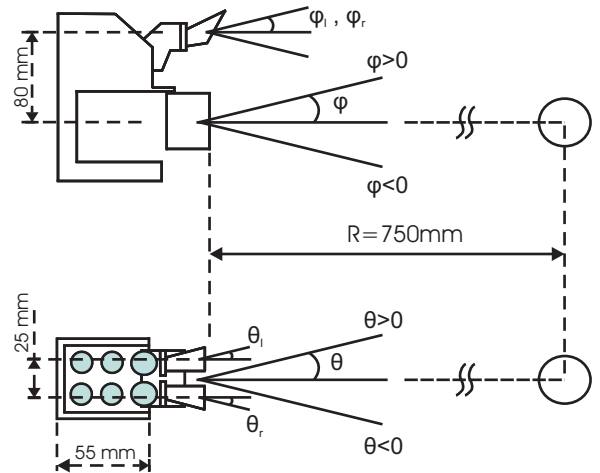


Figure 2: Schematic drawing of the measurement setup. θ (azimuth) and ϕ (elevation) represent target angles. Top: targets above the horizontal plane $\phi=0$ have positive ϕ -values. Bottom: targets on the side of the left ear with respect to the vertical plane $\theta=0$ have positive θ -values. The non-zero dimensions of the sonar head are known, therefore θ_l, θ_r , and ϕ_l, ϕ_r can be calculated from θ, ϕ and the distance to the reflector R .

2.2 Artificial Pinna: *Phyllostomus discolor*

Fig. 3 shows one of the artificial pinnae used in this research. A specimen of *Phyllostomus discolor* was scanned with a Skyscan 1076 μ -CT machine (details of this procedure can be found in (De Mey et al. 2008)). From this 3D-model, a single pinna was extracted and virtually mounted onto a support structure in such a way that its orientation matches that of the scanned *Phyllostomus discolor* head with respect to the $\phi=0^\circ$ elevation plane, defined by the eye-nostril line, and the $\theta=0^\circ$ azimuth plane, defined by the mid-sagittal plane. Two mirrored versions of this model were 3D-printed (an acrylic-based photopolymer) and in each of them a Knowles FG-23329 microphone was inserted at the end of the ear canal. Both artificial pinnae were then mounted on the sonar head with both support structures facing forward (directions $\theta_l=0^\circ$ and $\theta_r=0^\circ$ are parallel to $\theta=0^\circ$, directions $\phi_l=0^\circ$ and $\phi_r=0^\circ$ are parallel to $\phi=0^\circ$), so that the final orientations match those of the scanned *Phyllostomus discolor* head.

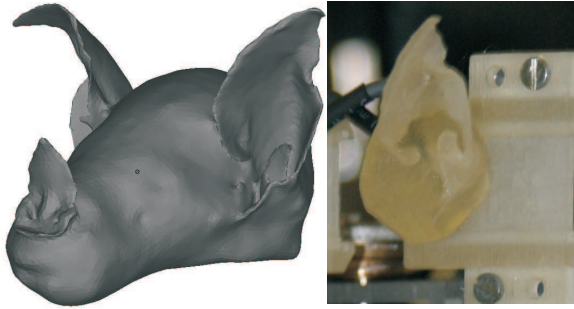


Figure 3: (a) Virtual 3D-model of scanned *Phyllostomus discolor* head. (b) the corresponding artificial pinna, which was cut from the virtual model, merged with a support structure model and finally 3D-printed

2.3 Spectral Code Extraction

The 3D-localization method presented here is based on spectral cues i.e., the direction-dependent changes in the echo spectra as a function of the reflector position. These echo spectra are represented by a spectral code that is extracted from the received wave forms. Note that we use the term 'spectral code' because the extraction method does not return the exact echo spectrum i.e., the Fourier transform of the returning wave form, but a close approximation instead.

The process of extracting the spectral code of a reflector that has been insonified with a frequency-modulated call, is described at length in (Reijniers & Peremans 2007). In the current paper, a 70-channel gammatone filterbank with center frequencies from 100kHz-30kHz and Q-factor 50 is used to construct a spectrogram of the echo signal (fig. 4b). By time shifting all frequency channels with a value corresponding to the frequency-dependent time delays in the emitted fm-call, a dechirped representation is constructed (fig. 4c). From this representation, the echo spectral code is extracted by selecting the values corresponding to the maximum summed energy of the dechirped spectrogram. Note that this scheme makes use of the prior knowledge of the time-frequency representation of the emitted call (cf. matched filter). Also, this method allows localization of multiple targets (when separated in distance) since one can extract multiple echo spectral codes from a single emission.

The current chirp pulse is a linear period modulated (the frequency is swept hyperbolically from 120kHz - 30kHz, with a duration of 3msec)

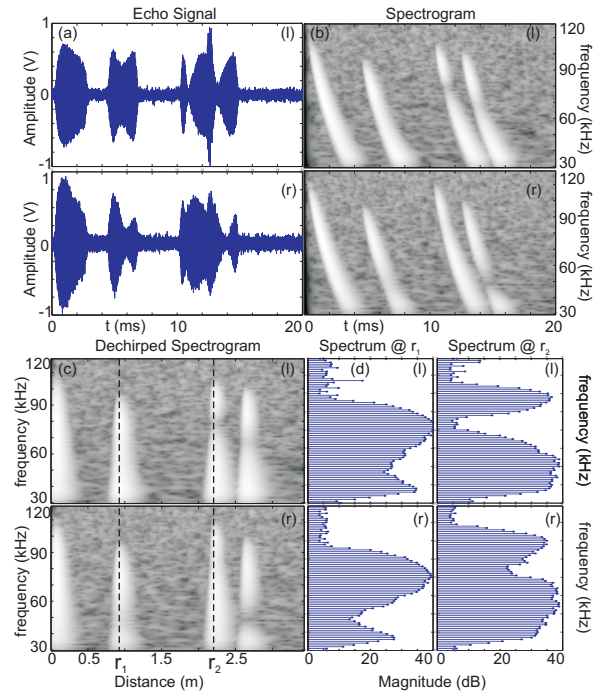


Figure 4: Visualization of the spectral code extraction method: (a) Wave form representing the picked up call and three echoes, with the last two overlapping in time. (b) Spectrogram representation of the gammatone filterbank response. Each echo is a filtered version of the emitted fm-call (c) The dechirping process aligns the individual frequency channel responses and separates spectra of echoes that partially overlap in time. (d) Two individual binaural spectral codes, extracted at distances r_1 and r_2 .

pulse which is quite typical for the vocalizations of so-called fm-bats i.e., bats with broadband calls (Thomas, Moss & Vater 2003). Because of the dechirping process, pulse overlap is not determined by chirp pulse length, but by the duration of the responses of the filters in the chosen filter bank, as illustrated in fig. 4.

In this study a single reflector was insonified, requiring no further focus of attention mechanism. Finally, the distances r_i to different targets are easily extracted from the dechirped spectrogram representation.

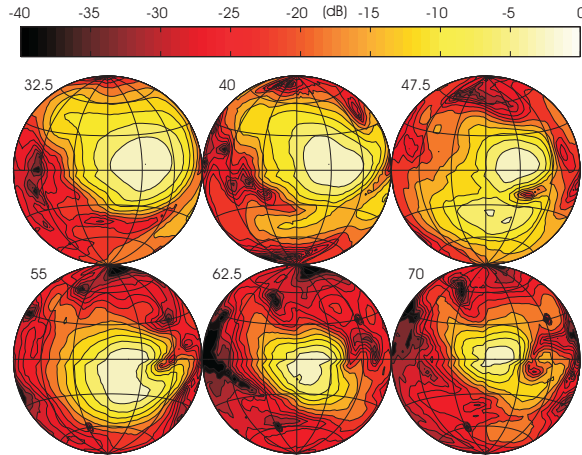


Figure 5: Shaded contour plots of the measured HRTF of the artificial *Phyllostomus discolor* left pinna (frequencies 32.5-70kHz in 7.5kHz-intervals). Each plot represents a spherical projection of the frontal hemifield ($\pm 90^\circ$ in both azimuth and elevation). Isocontour lines of the spectrum magnitude relative to the maximum magnitude at each frequency are shown in 3dB-decrements. The shading corresponds to relative magnitude, white being the largest and darkening with decreasing magnitude.

3 HRTF of the Artificial Pinna

Spectrum based localization relies on the direction-dependent spectral filtering performed by the pinna structures. This direction-dependent filtering is conventionally described by the head related transfer function (HRTF). The HRTF of the left artificial pinna was measured by directing a Polaroid-type transducer from different azimuth and elevation coordinates evenly spaced on a half sphere with radius 300 mm, centered around the fixed pinna (azimuth, elevation range: -90° to $+90^\circ$, interval 5°). From each position, a calibrated frequency modulated call, sweeping downward from 120kHz to 20kHz, 2ms long, was emitted. The frequency content of the impinging sound wave was analyzed with a 2000-point FFT. Fig 5 shows the results of the HRTF-measurement, represented by normalized surface plots of the spectrum magnitude in the observed area for a number of selected frequencies (32.5-70kHz, 7.5kHz interval).

The most sensitive regions lie between 0° and 60° azimuth in the bat's left hemifield (on the right hand side in fig. 5 for the reader) and -30° to 30° eleva-

tion. The sonar axis, defined as the most sensitive direction for a particular frequency, varies a great deal with frequency and effectively introduces both azimuth and elevation vergence in the binaural system. This scanning motion of the sonar axis has an important effect on the spatial cues in the echo signals. The main lobes, defined as the area within 3dB of the highest value, are irregularly shaped around these sonar axes and decrease in width with increasing frequency. Distinct side lobes, as seen at 47.5kHz in the southern half of the frontal hemifield, provide additional spatial cues. The combined effect of this direction-dependent filtering marks each impinging echo signal with a spatial signature that can be used for localization, as we will demonstrate.

Direction-dependent filtering by such an artificial bat pinna is much more complex than the basic sensitivity patterns of common ultrasonic transducers (Kinsler et al. 2000). The sensitivity of a conventional transducer (the so-called piston model) is described by an axisymmetrical main lobe centered on a fixed transducer axis, which decreases in width as frequency increases. Around this main lobe multiple side lobes appear, decreasing in width with increasing frequency and angle. However, such an axisymmetrical sensitivity pattern is highly ambiguous as all echoes coming from directions that make an angle α with the piston axis will result in equal spectra.

The difference between the axisymmetrical sensitivity pattern of conventional transducers and the much more complex 2D-transfer function of the artificial pinna raises some important questions. In the current paper we show that the pinna complexity allows discrimination between different reflector locations based on a binaural broadband spectrum. However, it is not yet fully clear which specific properties of the pinna HRTF allow this discrimination. It can be shown that binaural spectral information obtained from conventional transducers in the same configuration i.e., all three transducers pointing forward in the $(0^\circ, 0^\circ)$ -direction, is not sufficient for 3D-localization. However, simulation results show that a more intelligent configuration with conventional transducers can be devised that does provide sufficient binaural spectral cues for 3D-localization in a central part of the frontal hemifield. Nevertheless, we conjecture that the variation in sonar axis with frequency enables equally performant binaural spectrum-based 3D-localization with a less strict receiver configuration requirement, providing fur-

ther disambiguation options by allowing ear mobility. However, these preliminary analysis results require further investigation.

The HRTF-measurements were compared to results of an acoustic simulation of the corresponding (virtual) 3D-model and shown to be in good agreement (De Mey et al. 2008). Furthermore, it showed that spatial filtering is predominantly caused by the pinna shape, and that head or support structure effects are minor. The design of artificial pinnae should therefore focus on the pinna shape itself, and only to a lesser degree on the shape of the support structure.

4 The Active Head Related Transfer Function

Although the HRTF of a single pinna is an important factor in the direction-dependent filtering of sound waves returning from different reflector locations, its true influence on active binaural echolocation can only be investigated by taking into account the complete sound path i.e., including the transmitter radiation pattern, air filtering and reflector filtering.

4.1 Binaural Sound Path and AHRTF

The left and right receiver spectra S_l and S_r returning from a reflector at distance r , azimuth θ and elevation ϕ , in a noiseless environment, can be written as the result of a series of frequency-dependent spatial filter operations in the frequency domain:

$$S_l = H_l(\theta_l, \phi_l, f) \cdot H_a(r, f) \cdot H_{rfl}(\theta_l, \phi_l, f) \cdot X \quad (1)$$

$$S_r = H_r(\theta_r, \phi_r, f) \cdot H_a(r, f) \cdot H_{rfl}(\theta_r, \phi_r, f) \cdot X \quad (2)$$

with

$$X = H_a(r, f) \cdot H_{tr}(\theta, \phi, f) \cdot X_c(f) \quad (3)$$

where H_{tr} , H_a , H_{rfl} , H_l and H_r describe the filtering characteristics of transmitter, air, reflector, left and right receiver assembly respectively. Because the 3D-localization method does not use phase information, all frequency domain formulas in this paper describe magnitude effects only. Vertical bars are therefore omitted to shorten notation.

X is the spectrum of the sound wave reaching the reflector, which is in fact X_c , the spectrum of the emitted

call, filtered only by air H_a and the transmitter characteristic $H_{tr}(\theta, \phi, f)$. The received echo spectrum S_l i.e., the reflection of X directed at the left pinna (from angle θ_l and ϕ_l), additionally depends on reflector filtering $H_{rfl}(\theta_l, \phi_l, f)$, again air filtering H_a , and, finally, pinna filtering $H_l(\theta_l, \phi_l, f)$. The same holds true for the echo spectrum of the sound wave received by the right pinna, using the corresponding angles.

We introduce the concept of the Active Head Related Transfer Function (AHRTF) to describe the *direction-dependent* systematic spectral filtering performed by a particular binaural active echolocation system. It is denoted $H_A(\bar{\theta}, f)$, with $\bar{\theta} = (\theta, \phi)$ the target azimuth and elevation, and f a set of frequencies for which the system behavior is described. By definition:

$$H_A(\bar{\theta}, f) = [H_l(\bar{\theta}_l, f) \cdot H_{tr}(\bar{\theta}, f), H_r(\bar{\theta}_r, f) \cdot H_{tr}(\bar{\theta}, f)]. \quad (4)$$

Note that this definition entails the geometrical relationship between $\bar{\theta}_r$, $\bar{\theta}_l$ and $\bar{\theta}$, determined by the head dimensions and pinna orientations. From equations 1 through 3, we obtain the relationship between $H_A(\theta, \phi, f)$ and the received spectra S_l and S_r :

$$H_A(\bar{\theta}, f) = \left[\frac{S_l(r, \bar{\theta}, f)}{H_{rfl}(\bar{\theta}_l, f) H_a^2(r, f) X_c(f)}, \frac{S_r(r, \bar{\theta}, f)}{H_{rfl}(\bar{\theta}_r, f) H_a^2(r, f) X_c(f)} \right]. \quad (5)$$

The importance of the AHRTF lies in its spatial properties i.e., the variation of the spectrum magnitude for a given frequency as a function of the reflector location. These intra-frequency properties can be investigated without having to consider the inter-frequency properties of the received spectra i.e., the relative spectrum magnitudes across different frequencies for a given location, which are also dependent on the emitted call X_c and air filtering H_a .

4.2 Transmitter Directivity

H_A is dependent on H_{tr} . We therefore measured H_{tr} by positioning a receiver at different azimuth and elevation coordinates evenly spaced on a half sphere with radius 300 mm, centered around the fixed transmitter (azimuth, elevation range: -45° to $+45^\circ$, interval 1°). For each receiver position, a calibrated frequency modulated call, sweeping downward from 120kHz to 20kHz, 2ms long, was emitted. The frequency content of the

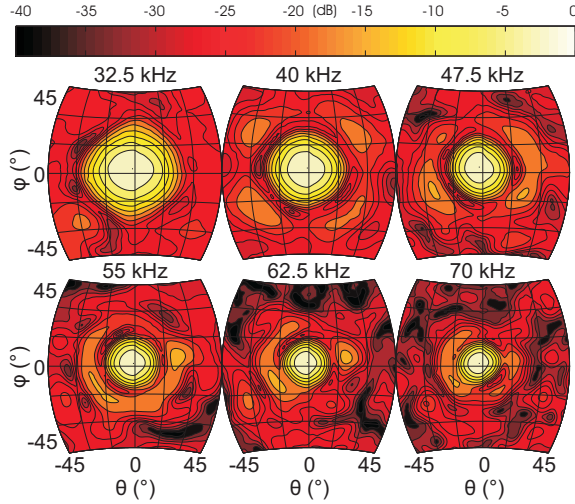


Figure 6: Shaded contour plots of H_{tr} , the measured directivity of the transmitter, shown for frequencies 32.5kHz-70kHz in 7.5kHz-intervals. Each plot represents a spherical projection of the frontal hemifield ($\pm 45^\circ$ in both azimuth and elevation). Isocontour lines of the spectrum magnitude relative to the maximum magnitude at each frequency are shown in 3dB-decrements. The shading corresponds to relative magnitude, white being the largest and darkening with decreasing magnitude.

impinging sound wave was analyzed with a 2000-point FFT. Results of the spatial dependency of the spectrum magnitude are shown in fig. 6 for a selection of frequencies.

Across all observed frequencies, the maximum magnitude is observed for a single central direction near $(\theta, \phi) = (0^\circ, 0^\circ)$, determining the transmitter main-directivity axis. The main lobe around this sonar axis rapidly decreases in size as frequency increases, as predicted by the piston-model. Also, at higher frequencies, side lobes appear as (intermittent) concentric circles around the sonar axis. Most energy is directed within a cone with top angle of 30° . The transmitter effectively acts as a focal mechanism. It should however be noted that bats can generate wide beams with much higher energy than the transducers currently available. Better transducers could greatly improve system performance.

4.3 AHRTF: Spatial Properties

The spatial properties of the AHRTF $H_A(\theta, \phi, f)$ i.e., the direction-dependent spectral filtering performed by a particular binaural active echolocation system, can be investigated through equation 5. In the special case of an ideal isotropic point reflector, reflector filtering H_{rfl} can be considered to be direction-independent. Air filtering H_a and the frequency content of the emitted call X_c are also direction-independent. Therefore the spatial properties of S_l and S_r also describe the spatial properties of the AHRTF.

The best approximation to such an isotropic point reflector with good reflector strength is a ball reflector. We therefore hung a wooden ball (70 mm diameter) at a distance of 750 mm in front of the sonar head. Then, we moved its neck from positions $\theta_{neck} = -45^\circ$ to $\theta_{neck} = +45^\circ$ (azimuth) and from $\phi_{neck} = -36^\circ$ to $\phi_{neck} = +36^\circ$ (elevation) in steps of 1° , corresponding to the head range-limits. From each of these positions, the robot head emitted a series of 100 frequency modulated calls sweeping downwards from 120kHz-30kHz with a duration of 3ms and for each corresponding target angle (θ, ϕ) the returning echo spectral codes S_l and S_r were extracted and stored. The spatial characteristics of the resulting mean spectral code set are visualized in fig. 7 and effectively describe the spatial properties of the AHRTF.

From the results shown in fig. 7 we conclude that the transmitter radiation pattern dominates the AHRTF characteristics. The shape and size of the central lobe of H_{tr} is clearly visible in each frequency of H_A . Comparing fig. 7 with fig. 6 and fig. 5, one sees how the pinna HRTF interacts with the transmitter radiation pattern. **The symmetry of the transmitter directivity is broken as the left pinna is much more sensitive for reflectors in the left hemifield. The direction of the sonar axis in the pinna HRTF and the region of high sensitivity around it determine the AHRTF region where combined sensitivity remains high for a given frequency. Less sensitive regions in the pinna HRTF become even more attenuated in the AHRTF. Note that the side lobe in the lower half of the frontal hemifield at 47.5k Hz in the pinna HRTF produces a region of relatively high sensitivity in the lower half of the AHRTF. The position of the central lobe is slightly shifted due to the pinna. For higher frequencies, the spectral code only contains above-noise values for θ and ϕ close to 0° , because much less energy is being emitted at these frequencies, and this energy**

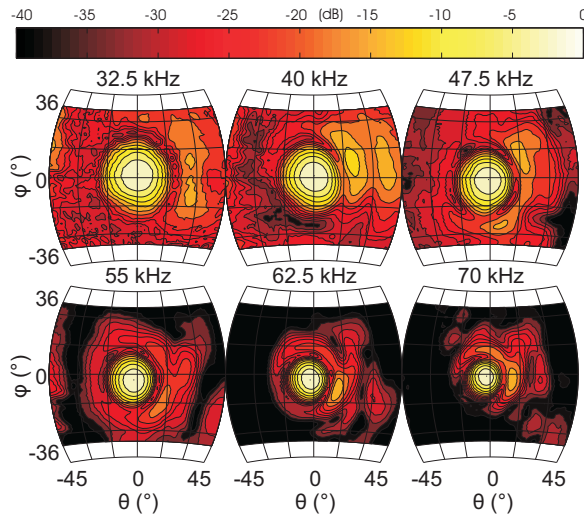


Figure 7: Shaded contour plots of the direction-dependent characteristics of the measured AHRTF (Left Pinna only) for the ball reflector (frequencies 32.5-70kHz in 7.5kHz-intervals). Each plot represents a spherical projection of the frontal hemifield ($\pm 45^\circ$ in azimuth, $\pm 36^\circ$ in elevation, interval size 1°). Isocontour lines of the spectral code magnitude relative to the maximum magnitude at each frequency are shown in 3dB-decrements.

is highly focused around the transmitter main-axis.

Interestingly, when looking at the AHRTF-characteristics for both ears, each area within the observable range features useful sensitivity for at least part of the relevant frequency range. As a result, the spectral codes returning from a reflector at different angles vary a great deal across the observed range and across frequencies. We hypothesize that the transmitter radiation pattern defines a focal area within which the pinna generates directional cues thereby enabling reflector localization.

Furthermore, a simulation of the AHRTF based on individual measurements of H_l , H_r , H_{tr} and the geometrical relationships of the head configuration confirmed that the ball reflector indeed approximates an isotropic point reflector well.

5 Spectrum based binaural 3D-Localization

The binaural 3D-localization method is based on the observation that echoes returning from reflectors at different locations in 3D-space have systematic variations across the relevant frequency spectrum.

In the previous sections, the intra-frequency properties of $H_A(\theta, \phi, f)$ were characterized and visualized. However, for localization purposes, one should consider the inter-frequency information contained in the broadband spectral codes for each (θ, ϕ) -pair as well. As stated earlier, these spectral codes are determined by the frequency characteristics of X_c , H_{tr} , H_a , X_{rfl} , and finally H_l and H_r .

The spectrum based 3D-localization method described here is based on the assumption that air filtering H_a , reflector filtering H_{rfl} , and distance effects (within limits) do not dominate the shape of the resultant spectral code. Furthermore, it assumes that, given a sufficiently complex directivity pattern of the various system components, the spatial signature of an impinging echo, and thus the reflector location, can be extracted.

The ball reflector best approximates the ideal isotropic reflector. Therefore, a set of binaural template spectra $T(\theta, \phi, f)$ was collected from 100 measurements on the ball for all target angles (θ_j, ϕ_k) . The individual template spectra $T(\theta_j, \phi_k, f)$ consist of the concatenation of the two monaural spectral codes S_l and S_r for that particular target angle (θ_j, ϕ_k) , forming a $2 \times 70 = 140$ dimensional vector.

After emission, a binaural spectral code is extracted from the echo signals returning from an unknown reflector location. Based on this binaural spectral code S_x (also the concatenation of the two monaural spectral codes S_l and S_r forming a $2 \times 70 = 140$ dimensional vector) the estimation method will search for the most probable target angle (θ, ϕ) from which the echo could have returned.

Each stored spectral template $T(\theta_j, \phi_k, f)$ is first normalized to the energy of S_x , resulting in the normalized template set $T_x(\theta, \phi, f)$. Let N be the number of frequency bands of the gammatone filterbank and f the vector of corresponding center frequencies. $\bar{\theta}_{jk}$ is short notation for the azimuth-elevation pair (θ_j, ϕ_k) . Then $\forall j, k$:

$$T_x(\bar{\theta}_{jk}, f) = \frac{|T(\bar{\theta}_{jk}, f)| \sqrt{\sum_{i=1}^{i=2N} |S_x(f_i)|^2}}{\sqrt{\sum_{i=1}^{i=2N} |T(\theta_{jk}, f_i)|^2}} \quad (6)$$

This normalization step is a first order approximation to compensate for unknown reflector strength and spherical spreading losses.

Next, every normalized template spectrum $T_x(\theta_j, \phi_k, f)$ is compared to the spectral code of the unknown reflector. Based on empirical evidence, we assume a normal distribution of the spectral code magnitude (log-values) around the expected value T_x . $\forall j, k$:

$$P(S_x | \bar{\theta}_{jk}) = C e^{-\frac{[S_x^{log} - T_x^{log}]^T \Sigma^{-1} [S_x^{log} - T_x^{log}]}{2}}$$

with

$$S_x^{log} = 20 \log_{10}(S_x(f))$$

$$T_x^{log} = 20 \log_{10}(T_x(\bar{\theta}_{jk}, f))$$

$$C = \frac{1}{(|\Sigma| (2\pi)^N)^{\frac{1}{2}}} \quad (7)$$

where Σ represents the covariance matrix containing information on the expected spectral variations. Σ was constructed by accumulating experimental data i.e., spectral codes extracted from measurements on various reflectors in various angles.

Finally, the reflector angle is estimated by selecting the maximum a posteriori probability using Bayes' theorem

$$\hat{\theta} = \text{max}_{\bar{\theta}} [P(\bar{\theta} | S_x)] = \text{max}_{\bar{\theta}} \left[\frac{P(S_x | \bar{\theta}) P(\bar{\theta})}{P(S_x)} \right] \quad (8)$$

$P(S_x)$ can be written as

$$P(S_x) = \sum_{jk=start}^{jk=end} P(S_x | \bar{\theta}_{jk}) P(\bar{\theta}_{jk}). \quad (9)$$

Without more specific prior information, $P(\bar{\theta})$ is assumed to be uniform. In that case, the probability density function $P(\bar{\theta} | S_x)$ is proportional to $P(S_x | \bar{\theta})$ (Altes 1978), (Schillebeeckx, Reijniers & Peremans 2008), and

$$\hat{\theta} = \text{max}_{\bar{\theta}} [P(\bar{\theta} | S_x)] = \text{max}_{\bar{\theta}} [P(S_x | \bar{\theta})] \quad (10)$$

i.e., the maximum likelihood estimator. Results of applying this procedure to the 3D-localization of various reflectors are described in the next section.

6 Binaural 3D-Localization: Results

6.1 3D-Localization: Various Reflectors

The 3D-localization procedure was tested by localizing 3 different reflectors, shown in fig. 8. The ball reflector is the reflector that was used to construct the template set $T(\theta, \phi, f)$. The blocks reflector was made from toy building blocks to obtain a multi-faceted reflector roughly the same size as the wooden ball, but with much more pronounced filtering characteristics. The crumpled paper ball serves as an example of a reflector class with a lot of stochastically distributed surfaces. **Example spectra to illustrate a realistic amount of unknown reflector filtering caused by the (randomly) chosen complex reflectors are shown in fig. 8.**

6.2 Known Reflector Filtering: Ball Reflector

6.2.1 Single Estimates

Fig. 9 illustrates four 3D-location estimates for four individual ball target angles. Each of the four estimates compares the extracted binaural spectral code S_1 i.e., the spectral code obtained from a single reading, to all available template spectra $T(\theta, \phi, f)$, using formulas 6 through 10, resulting in a $P(\bar{\theta} | S_1)$ -value for each candidate $\bar{\theta}$. The success of the estimation process depends on the resemblance between the measurement and the correct template spectrum.

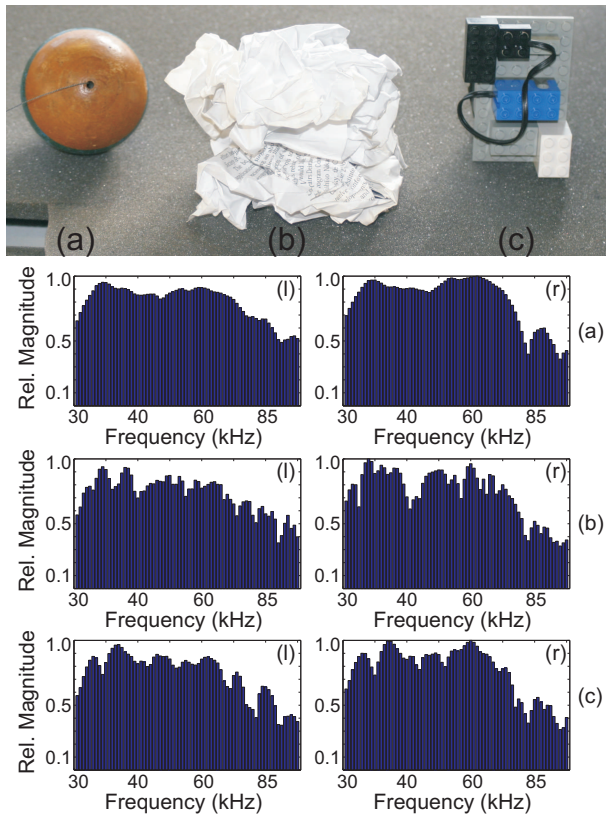


Figure 8: The three reflectors and **corresponding bin-aural example spectra**: (a) wooden ball , (b) crumpled paper, (c) blocks reflector. All three example spectra were extracted from a single reading of the reflector at angle $(\theta, \phi)=(0^\circ, 0^\circ)$ and normalized to the maximum spectrum magnitude.

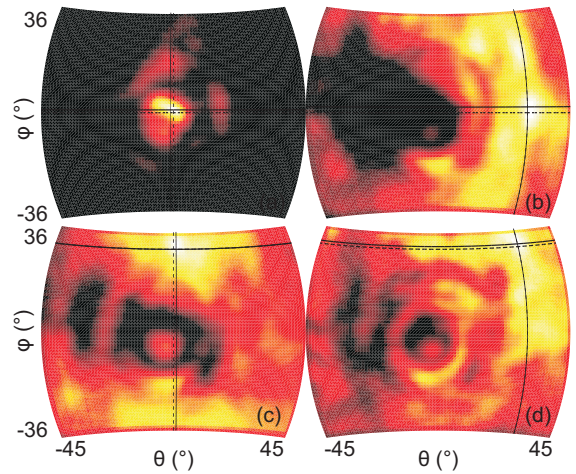


Figure 9: Single estimation results for a single reading of the ball reflector depicting $\log_{10}(P(\theta|S_1))$ for all considered θ . The shading corresponds to relative probability, white being the highest and darkening with decreasing probability. The correct angle (θ_j, ϕ_k) is located on the intersection of the dashed lines. The estimated angle $(\hat{\theta}, \hat{\phi})$ is located on the intersection of the full lines. (a) $(\theta_j, \phi_k)=(0^\circ, 0^\circ), (\hat{\theta}, \hat{\phi})=(-1^\circ, 1^\circ)$
(b) $(\theta_j, \phi_k)=(30^\circ, 0^\circ), (\hat{\theta}, \hat{\phi})=(30^\circ, 2^\circ)$
(c) $(\theta_j, \phi_k)=(0^\circ, 30^\circ), (\hat{\theta}, \hat{\phi})=(1^\circ, 30^\circ)$
(d) $(\theta_j, \phi_k)=(30^\circ, 30^\circ), (\hat{\theta}, \hat{\phi})=(30^\circ, 31^\circ)$

A clear match between the measurement spectral code S_1 and the template spectral code at the correct angle (θ_j, ϕ_k) results in a distinct maximum, as seen in fig. 9a and fig. 9c. Poorer resemblance due to noise conditions creates a larger area of uncertainty around the correct (θ_j, ϕ_k) -angle and can produce ambiguous regions where template spectral codes are similar to S_1 . In fig. 9b and fig. 9d such regions appear, but the selected location (maximum $P(\hat{\theta}|S_1)$ -value) is still very close to the correct target angle.

6.2.2 Full Range Estimates

A more complete test was performed by localizing the ball reflector from all neck positions within the sonar head range. Target angles varied from $\theta=45^\circ$ to $\theta=-45^\circ$ and $\phi=36^\circ$ to $\phi=-36^\circ$, in steps of 1° . For each of these 6643 target angles, a spectral code S_1 was extracted from a single reading and the template angle (θ, ϕ) with maximum $P(\hat{\theta}|S_1)$ -value was selected as the estimate $(\hat{\theta}, \hat{\phi})$. Results are shown in fig. 10.

3D-localization of the wooden ball is highly accurate within the observed range, but this can be expected as it is the same reflector that was used to build the template set $T(\theta, \phi, f)$. The ball target is accurately located ($|\hat{\theta} - \bar{\theta}| \leq 3^\circ$) for just under 88% of all angles. The 95%-mark is reached at $|\hat{\theta} - \bar{\theta}| \leq 6^\circ$. 2.5% of all angles are badly estimated ($|\hat{\theta} - \bar{\theta}| \geq 10^\circ$). Note that the measurements resulting in test set S_1 were carried out separately from those resulting in the template set $T(\theta, \phi, f)$. The majority of the poor estimations is scattered around the outer regions of the field of view ($|\theta| \geq 30^\circ$), where SNR is much lower than in the central area.

From the single estimations shown in fig. 9 it is apparent that more noise results in more ambiguous regions and less distinct maxima around the correct angle, reducing the probability that the target angle is correctly estimated. However, these numbers show that reflector 3D-localization based on spectral cues is achievable in realistic noise conditions and within a large field of view.

Furthermore, it should be noted that by selecting only the target angle with maximum $P(\hat{\theta}|S_1)$ -value, a lot of information about the distribution of $P(\theta|S_1)$ is lost. More intelligent schemes that make use of all information in the $P(\theta|S_1)$ distribution can be envisaged. (Todo: eventuele verdere bespreking van de mogelijke technieken in antwoord op reviewer-vraag?)

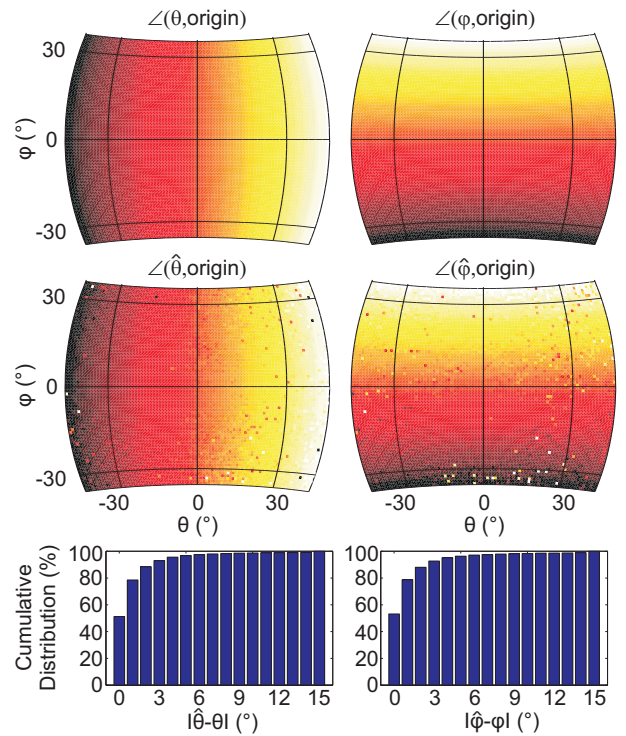


Figure 10: Results showing spatial distribution and cumulative error distribution of the ball target estimates $\hat{\theta}$ (left) and $\hat{\phi}$ (right) within the range $\theta=45^\circ$ to $\theta=-45^\circ$ and $\phi=36^\circ$ to $\phi=-36^\circ$, in steps of 1° : (top) reference results showing the color coding for the correct azimuth angles θ and elevation angles ϕ , (middle) azimuth estimates $\hat{\theta}$ and elevation estimates $\hat{\phi}$ for all ball target angles (θ, ϕ) , (bottom) cumulative distributions for the azimuth and elevation errors.

6.3 Unknown Reflector Filtering

The measurements were repeated with two other reflectors (see fig. 8) to illustrate the impact of unknown reflector filtering on binaural spectrum-based localization. These estimates were carried out with the template set $T(\theta, \phi, f)$ and Σ that was used in the ball target estimates shown in the previous section.

6.3.1 Single Estimates

Fig. 11 shows eight single estimates i.e., the two reflectors in the same four target angles as in fig. 9. For each of these estimates, a spectral code S_1 was extracted from a single reading.

Again, a close match results in a distinct maximum near the correct angle (θ_j, ϕ_k) , as seen in fig. 11a, e and g. Larger areas of uncertainty around the correct (θ_j, ϕ_k) -angle are introduced in fig 11b, c, d, f and h. In the case of fig 11d, f and h ambiguous regions around incorrect target angles also appear. Estimates for fig. 11b, c, d and f are good i.e., the most likely target angle is found in the region around the correct (θ_j, ϕ_k) and both azimuth and elevation errors are small. However, probabilities in the ambiguous regions are only slightly lower than that of the selected angle. In fig. 11h the maximum probability is reached in such an ambiguous region leading to a large estimation error. These results illustrate how noise conditions and/or outspoken reflector filtering can affect target localization.

6.3.2 Full Range Estimates: Reflector Filtering

To investigate which part of the performance loss can be attributed to reflector filtering and noise conditions, respectively, a set of high SNR spectral codes S_{100} was constructed for both complex reflectors, simulating the spectral code that would be extracted with a high-SNR acquisition system in noiseless conditions. These spectral codes were constructed by averaging over the spectra extracted from 100 consecutive readings of the stationary target for each target angle within the neck range. It should be noted that the orientation of the reflector changes only slightly when viewed from these different angles. The results should therefore be seen as an illustration rather than a full analysis of the effect of reflector filtering.

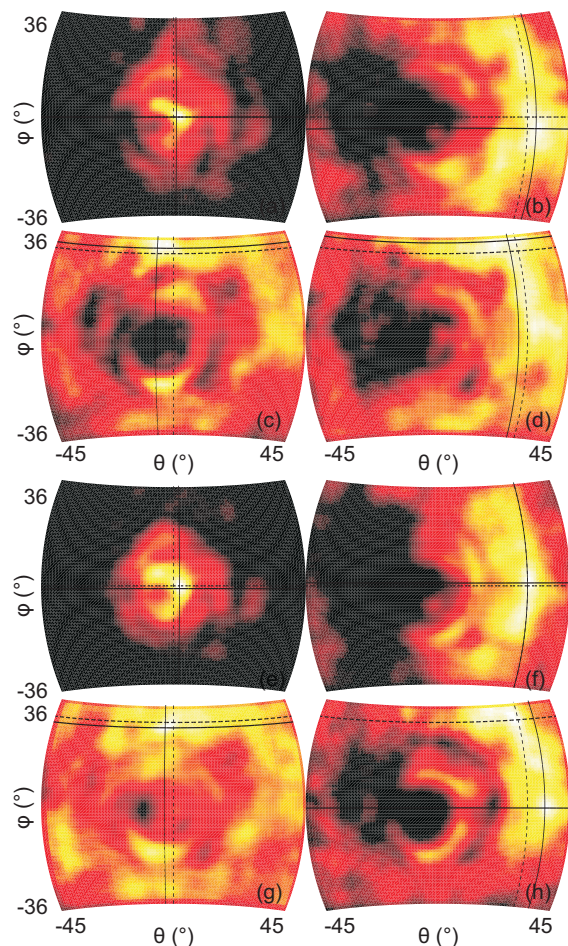


Figure 11: Single estimation results for the blocks and crumpled paper reflector depicting $\log_{10}(P(\hat{\theta}|S_1))$ for all considered $\hat{\theta}$. The shading corresponds to relative probability, white being the highest and darkening with decreasing probability. The correct angle (θ_j, ϕ_k) is located on the intersection of the dashed lines. The estimated angle $(\hat{\theta}, \hat{\phi})$ is located on the intersection of the full lines. (a) to (d) show results for the blocks reflector. (e) to (h) show results for the crumpled paper reflector. (a) $(\theta_j, \phi_k)=(0^\circ, 0^\circ), (\hat{\theta}, \hat{\phi})=(1^\circ, 0^\circ)$ (b) $(\theta_j, \phi_k)=(30^\circ, 0^\circ), (\hat{\theta}, \hat{\phi})=(33^\circ, -4^\circ)$ (c) $(\theta_j, \phi_k)=(0^\circ, 30^\circ), (\hat{\theta}, \hat{\phi})=(-6^\circ, 32^\circ)$ (d) $(\theta_j, \phi_k)=(30^\circ, 30^\circ), (\hat{\theta}, \hat{\phi})=(27^\circ, 34^\circ)$ (e) $(\theta_j, \phi_k)=(0^\circ, 0^\circ), (\hat{\theta}, \hat{\phi})=(2^\circ, -1^\circ)$ (f) $(\theta_j, \phi_k)=(30^\circ, 0^\circ), (\hat{\theta}, \hat{\phi})=(30^\circ, 1^\circ)$ (g) $(\theta_j, \phi_k)=(0^\circ, 30^\circ), (\hat{\theta}, \hat{\phi})=(-3^\circ, 28^\circ)$ (h) $(\theta_j, \phi_k)=(30^\circ, 30^\circ), (\hat{\theta}, \hat{\phi})=(36^\circ, -1^\circ)$

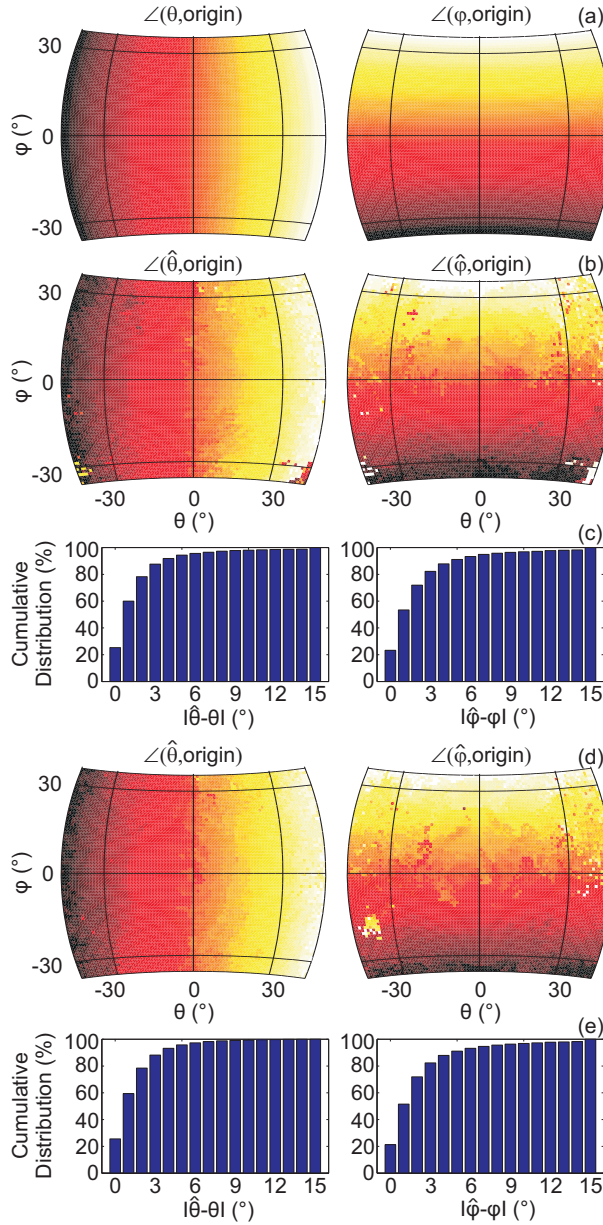


Figure 12: Results showing spatial distribution and cumulative error distribution of the blocks and crumpled paper target estimates $\hat{\theta}$ (left) and $\hat{\phi}$ (right) within the range $\theta=45^\circ$ to $\theta=-45^\circ$ and $\phi=36^\circ$ to $\phi=-36^\circ$, in steps of 1° based on the S_{100} -spectrum: (a) reference results showing the color coding for the correct azimuth angles θ and elevation angles ϕ , (b) azimuth estimates $\hat{\theta}$ and elevation estimates $\hat{\phi}$ for all blocks target angles (θ, ϕ) , (c) **cumulative distributions** for the azimuth and elevation errors for the blocks reflector, (d) azimuth estimates $\hat{\theta}$ and elevation estimates $\hat{\phi}$ for all crumpled paper target angles (θ, ϕ) , (e) **cumulative distributions** for the azimuth and elevation errors for the crumpled paper reflector.

Fig. 12b and c show the results for the block reflector set S_{100} . There is a clear systematic correspondence between the estimations and correct angles, both in azimuth and elevation, although results are generally less accurate in elevation than in azimuth. Due to reflector filtering and the resultant difference between the spectral codes for the blocks reflector and those for the wooden ball reflector, estimation errors become larger, as can be expected. In the outer regions ($\bar{\theta} \geq 30^\circ$), one detects a few contiguous areas where angle estimation is poor, due to ambiguous regions in $P(\bar{\theta}|S_{100})$ with maxima further away from the correct $\bar{\theta}_{jk}$. Nonetheless, 73% of all target angles are estimated with an error $\hat{\theta} - \bar{\theta} \leq 3^\circ$, and just under 90% with an error $\hat{\theta} - \bar{\theta} \leq 6^\circ$. These percentages increase as the reflector is more centrally located in the field of view. 5% of all target angles are falsely located ($\hat{\theta} - \bar{\theta} \geq 10^\circ$).

These results are corroborated by the results of the crumpled paper estimation (fig.12d and e). Results are similar to the ones obtained with the blocks reflector. Over 73% of all target angles are estimated with an error $\hat{\theta} - \bar{\theta} \leq 3^\circ$ and just over 90% of all target angles with an error $\hat{\theta} - \bar{\theta} \leq 6^\circ$. 4% is falsely located ($\hat{\theta} - \bar{\theta} \geq 10^\circ$). Overall, azimuth results are much better than elevation estimations, predominantly because the combined binaural spectrum also codes for IID-cues (interaural intensity differences). In effect, the binaural spectrum cues can be considered a superset of the IID-cues.

From these results, we conclude that the echo spectrum is dominated by the direction-dependent spectral filtering as described by the AHRTF H_A , and not by reflector filtering. Therefore, the binaural echo spectrum is a valid 3D-localization cue for complex reflectors as well.

6.3.3 Full Range Estimates: Added Noise

Results for test sets S_1 for both the blocks and the crumpled ball reflector show the effect of added noise on top of unknown reflector filtering (fig. 13). As can be expected for individual estimations, the performance level drops. The probability increases that the noisy spectrum is more similar to a wrong template spectrum than to the one that corresponds with the correct angle.

In the case of the blocks reflector (fig.13b and c), 48% of all target angles are estimated with an error $\hat{\theta} - \bar{\theta} \leq 3^\circ$. Just over 70% of all angles with an error $\hat{\theta} - \bar{\theta} \leq 6^\circ$. In 20%, a false template spectrum has

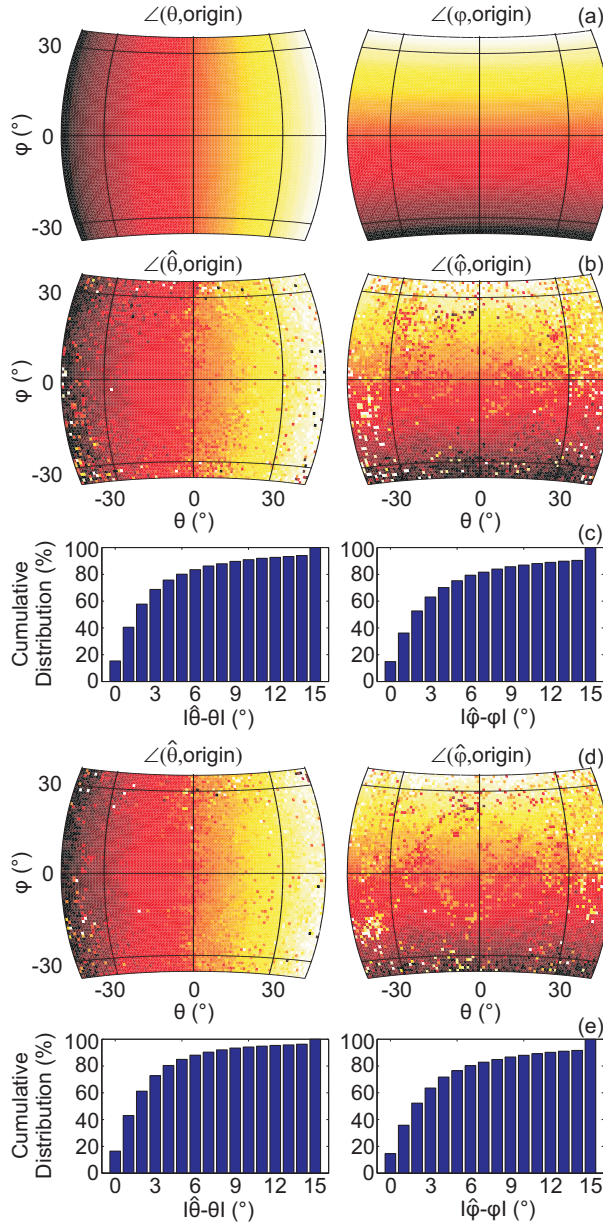


Figure 13: Results showing spatial distribution and cumulative error distribution of the blocks and crumpled paper target estimates $\hat{\theta}$ (left) and $\hat{\phi}$ (right) within the range $\theta=45^\circ$ to $\theta=-45^\circ$ and $\phi=36^\circ$ to $\phi=-36^\circ$, in steps of 1° based on the S_1 -spectrum: (a) reference results showing the color coding for the correct azimuth angles θ and elevation angles ϕ , (b) azimuth estimates $\hat{\theta}$ and elevation estimates $\hat{\phi}$ for all blocks target angles (θ, ϕ) , (c) cumulative distributions for the azimuth and elevation errors for the blocks reflector, topped at 15° -error, (d) azimuth estimates $\hat{\theta}$ and elevation estimates $\hat{\phi}$ for all crumpled paper target angles (θ, ϕ) , (e) cumulative distributions for the azimuth and elevation errors for the crumpled paper reflector, topped at 15° -error.

a higher probability than the template spectrum at the correct target angle, leading to a large estimation error.

The crumpled paper ball results (fig.13d and e) are again similar: 50% of all angles are estimated with an error $\hat{\theta} - \bar{\theta} \leq 3^\circ$. 74% have an error $\hat{\theta} - \bar{\theta} \leq 6^\circ$. 15% are badly estimated ($\hat{\theta} - \bar{\theta} \geq 10^\circ$).

From these measurements, we conclude that **3D-localization of various targets based on spectral information from a single measurement is possible under realistic noise conditions. However, results are noise-dominated and therefore unreliable. Evidently, all measures that increase the system's SNR will result in better localization performance. With the current system, a single measurement estimate can only be sufficiently accurate if favorable SNR-conditions are present. Indeed, as shown by the difference between the S_1 and S_{100} results, the inaccuracy of the single estimates for the complex reflectors is to a large extent due to the low SNR. Under high-SNR conditions, the S_{100} -spectra would actually resemble the spectra extracted from a single measurement, resulting in much better localization performance.**

However, because the spectral signature of the correct angle is present in the received echo signal, probabilities in the correct region should be only slightly smaller than those around the selected (θ, ϕ) -candidate, and much higher than those in all non-ambiguous regions. While the probability distribution is of no assistance to a single estimation that selects the maximum probability, it can be very helpful prior information to succeeding estimations and allows sequential estimation. Although a more elaborate discussion on these sequential techniques falls outside the scope of the current paper, it can be shown that two or three consecutive measurements are required to attain accurate localization for the current low SNR-conditions.

7 Discussion and Conclusions

Different bat species have evolved a wide range of pinna shapes, indicating that there is a large solution domain of pinna shapes that can solve the target localization problem (as well as target identification, a problem much less understood). Complex pinna filtering can be considered a form of analog computing, adding spatial information to received echo signals in real-time. One could say that they are the fixed-form counterpart of a

sensor array (Webb & Wykes 1996). Although such arrays give the sensor designer the flexibility to change the directional properties, it comes at a certain signal processing cost. Complex pinnae perform this spatial filtering free of charge, and in that sense, they serve as "advanced sensor arrays that allow feature discrimination and precise localization from a single vehicle location", as proposed by (Tardos et al. 2002).

In this study, it has been shown that an advanced sonar sensor equipped with complex pinnae can localize a reflector in 3D-space because the corresponding echo spectral code is dominated by the system's direction-dependent spectral filtering, as described by the AHRTF. Results show that this spatial signature can not only be extracted from measurements on the same object that was used to create the template set, it is a valid 3D-localization cue for complex reflectors as well.

Measurements of the AHRTF-properties indicate that it is desirable to examine the full binaural sound path, not the HRTF-properties of an individual pinna alone, when making predictions about the system's localization performance. This localization performance is largely determined by the transmitter radiation pattern, the pinna directivity and the interaction between them. The shape of the artificial pinna is based on a specimen of *Phyllostomus discolor*. No assumption is made about the optimality of the pinna shape of this particular bat species.

A Bayesian model is used to derive the target angle probability distribution within the observable range based on the similarity between the measurement spectrum and template set spectra. Although the single estimation method selects the target angle with maximum probability only, it provides useful prior information for consecutive estimations.

The Circe sonar head is a mechanically complex system. However, the localization method described here does not require pinna movement. Therefore, this binaural sonar system can be redesigned into a small and cheap sensor with a large information rate, using readily-available technology. Ear mobility could allow a further performance increase by reducing ambiguities, but this flexibility comes at the cost of more complex mechanics and increased size. However, it seems probable that by moving its head/ears, a bat actively shifts its focus of attention toward areas with a specific spatial activity across the relevant frequency range. An advanced sonar sensor, given enough degrees of freedom, could actively pursue such a strategy.

The binaural spectral codes on which the localization

method is based, are extracted from the echo signals with a scheme that makes use of the prior knowledge of the time-frequency representation of the emitted call, allowing localization of multiple targets with one measurement. The binaural sonar system is an active sensor: the spectral content of the emitted call is known, and could be adapted for specific tasks, although, in this research, one specific call was selected. **Many future research questions are raised, such as how best to configure the pinnae shape to maximize angular discrimination, how to optimize the transmitted chirp for discrimination, and possibly how to match the emitted call to a particular pinna shape. Also, current technology does not match the emitted energy and beamwidth of sound emissions by bats. Better transducer technology would greatly enhance performance.**

Mobile robot navigation performance depends on the quality of the system's sensory inputs. Therefore, the search for sensors that provide a large information rate i.e., accurate information within a large field of view at a high measurement rate, continues. We have demonstrated that it is possible to advance the potential of ultrasonic sensors by enhancing their directional properties by means of bio-inspired artificial pinnae. This enhanced directionality allows 3D-localization of real reflectors with a single, binaural active sonar measurement, in realistic noise conditions. In that sense, we believe the sonar system presented here is an example of how technical systems can benefit from knowledge and ideas derived from observing biological systems.

(bedanken van reviewers?)

8 Acknowledgments

This work was supported by the EU, IST-FET Program, as part of the CILIA [grant number FP6-016039] and ChiRoPing [grant number IST-215370] projects; the University of Antwerp BOF-UA Program supporting interdisciplinary Ph.D-research.

References

- Abdalla, H. & Horiuchi, T. K. (2008). Binaural spectral cues for ultrasonic localization, *Proc. of 2008 IEEE Int. Symp. on circuits and systems* **1-10**: 2110–2113.

- Akbarally, H. & Kleeman, L. (1995). A sonar sensor for accurate 3d target localisation and classification, *Proceedings of 1995 IEEE Int. Conf. on robotics and automation* **1-3**: 3003–3008.
- Altes, R. A. (1978). Angle estimation and binaural processing in animal echolocation, *Journal of the Acoustical Society of America* **63**(1): 155–173.
- Ayrulu, B. & Barshan, B. (1998). Identification of target primitives with multiple decision-making sonars using evidential reasoning, *International Journal of Robotics Research* **17**(6): 598–623.
- Barshan, B. (2007). Directional processing of ultrasonic arc maps and its comparison with existing techniques, *International Journal of Robotics Research* **26**(8): 797–820.
- Barshan, B. & Kuc, R. (1992). A bat-like sonar system for obstacle localization, *IEEE Transactions on Systems, Man and Cybernetics* **22**(4): 636–646.
- Barshan, B. & Sekmen, A. S. (1999). Radius of curvature estimation and localization of targets using multiple sonar sensors, *Journal of the Acoustical Society of America* **105**(4): 2318–2331.
- Biber, C., Ellin, S., Shenk, E. & Stempeck, J. (1980). The polaroid ultrasonic ranging system, *67th Convention of the Audio Engineering Society*.
- Chong, K. S. & Kleeman, L. (1999a). Feature-based mapping in real large scale environments using an ultrasonic array, *International Journal of Robotics Research* **18**(1): 3–19.
- Chong, K. S. & Kleeman, L. (1999b). Mobile-robot map building from an advanced sonar array and accurate odometry, *International Journal of Robotics Research* **18**(1): 20–36.
- De Mey, F., Reijniers, J., Peremans, H., Otani, M. & Firzlaff, U. (2008). Simulated head related transfer function of the phyllostomid bat *Phyllostomus discolor*, *Journal of the Acoustical Society of America* **124**(4): 2123–2132.
- Gao, W. & Hinders, M. (2006). Mobile robot sonar backscatter algorithm for automatically distinguishing walls, fences, and hedges, *International Journal of Robotics Research* **25**(2): 135–145.
- Keyrouz, F., Diepold, A. & Keyrouz, S. (2007). Robotic binaural and monaural information fusion using bayesian networks, *2007 IEEE International Symposium on Intelligent Signal Processing* pp. 285–290.
- Kinsler, L., Frey, A., Coppers, A. & Sanders, J. (2000). *Fundamentals of Acoustics*, 4 edn, Chapman and Hall, London, UK.
- Kleeman, L. (2004). Advanced sonar with velocity compensation, *Int. Journal of Robotics Research* **23**(2): 111–126.
- Kleeman, L. & Kuc, R. (1995). Mobile robot sonar for target localization and classification, *Int. Journal of Robotics Research* **14**(4): 295–318.
- Kuc, R. (1993). Three-dimensional tracking using qualitative bionic sonar, *Robotics and Autonomous Systems* **11**(3-4): 213–219.
- Kuc, R. (1994). Sensorimotor model of bat echolocation and prey capture, *Journal of the Acoustical Society of America* **96**(4): 1965–1978.
- Kuc, R. (2002). Binaural sonar electronic travel aid provides vibrotactile cues for landmark, reflector motion and surface texture classification, *IEEE Transactions on Biomedical Engineering* **10**(49): 1173–1180.
- Müller, R. & Kuc, R. (2007). Biosonar-inspired technology: goals, challenges and insights, *Bioinspiration and Biomimetics* **2**(4): 146–161.
- Obrist, M. K., Fenton, M. B., Eger, J. L. & Schlegel, P. A. (1993). What ears do for bats - a comparative study of pinna sound pressure transformation in chiroptera, *Jour. of Experimental Biology* **180**: 119–152.
- Peremans, H., Audenaert, K. & Van Campenhout, J. (1993). A high-resolution sensor based on tri-aural perception, *IEEE Transactions on Robotics and Automation* **9**(1): 36–48.
- Peremans, H. & Reijniers, J. (2005). *The CIRCE head: a biomimetic sonar system*, Vol. LNCS-3696, Springer Verlag, Berlin, DE.
- Peremans, H., Walker, V. A. & Hallam, J. C. T. (1998). 3d object localisation with a binaural sonarhead, inspirations from biology, *Int. Conf on Robotics and Automation* pp. 2795–2800.

- Pye, J., Flinn, M. & Pye, A. (1962). Correlated orientation sounds and ear movements of horseshoe bats, *Nature* **196**: 1186–1188.
- Reijniers, J. & Peremans, H. (2007). Biomimetic sonar system performing spectrum-based localization, *IEEE Transactions on Robotics* **23**(6): 1151–1159.
- Rodemann, T., Ince, G., Joublin, F. & Goerick, C. (2008). Using binaural and spectral cues for azimuth and elevation localization, *Int. Conf. on Intelligent Robots and Systems* pp. 2185–2190.
- Schillebeeckx, F., Reijniers, J. & Peremans, H. (2008). Probabilistic spectrum based azimuth estimation with a binaural robotic bat head, *Proceedings of the Fourth International Conference on Autonomous and Autonomous Systems* pp. 142–147.
- Shinn-Cunningham, B. G., Santarelli, S. & Kopco, N. (2000). Tori of confusion: Binaural localization cues for sources within reach of a listener, *Journal of the Acoustical Society of America* **107**(3): 1627–1636.
- Tardos, J., Neira, J., Newman, P. & Leonard, J. (2002). Robust mapping and localization in indoor environments using sonar data, *International Journal of Robotics Research* **21**(4): 311–330.
- Thomas, J., Moss, C. & Vater, M. (2003). *Echolocation in Bats and Dolphins*, University of Chicago Press.
- Thrun, S. (2001). A probabilistic on-line mapping algorithm for teams of mobile robots, *Int. Journal of Robotics Research* **20**(5): 335–363.
- Webb, P. & Wykes, C. (1996). High-resolution beam forming for ultrasonic arrays, *IEEE Transactions on Robotics and Automation* **12**(1): 138–146.
- Wotton, J. & Simmons, J. A. (2000). Spectral cues and perception of the vertical position of targets by the big brown bat, *eptesicus fuscus*, *Journal of the Acoustical Society of America* **107**(2): 1034–1041.